Journal of Marine Science and Technology

Volume 26 | Issue 2 Article 1

THERMAL PERFORMANCE IMPROVEMENT BY SPIKY TWISTED TAPES FOR LOOP THERMOSYPHON WITH NCG

Shyy Woei Chang
Department of System and Naval Mechatronic Engineering, National Cheng Kung University, Tainan, Taiwan, R.O.C, swchang@mail.ncku.edu.tw

Wei Ling Cai
Depart Department of System and Naval Mechatronic Engineering, National Cheng Kung University, Tainan, Taiwan, R.O.C

Recommended Citation

Chang, Shyy Woei and Cai, Wei Ling (2018) "THERMAL PERFORMANCE IMPROVEMENT BY SPIKY TWISTED TAPES FOR LOOP THERMOSYPHON WITH NCG," *Journal of Marine Science and Technology*: Vol. 26: Iss. 2, Article 1.
DOI: 10.6119/JMST.2018.04_(2).0001
Available at: https://jmstt.ntou.edu.tw/journal/vol26/iss2/1

THERMAL PERFORMANCE IMPROVEMENT BY SPIKY TWISTED TAPES FOR LOOP THERMOSYPHON WITH NCG

Acknowledgements

This work was financially supported by grant no. MOST105- 2221-E-022-002 from the Ministry of Science and Technology, Taiwan, and AVC Company

Journal of Marine Science and Technology, Vol. 26, No. 2, pp. 145-158 (2018)
DOI: 10.6119/JMST.2018.04_(2).0001

THERMAL PERFORMANCE IMPROVEMENT BY SPIKY TWISTED TAPES FOR LOOP THERMOSYPHON WITH NCG

Shyy Woei Chang[1] and Wei Ling Cai[2]

Key words: swirl evaporator, loop thermosyphon.

ABSTRACT

Thermal performance improvement for a two-phase loop thermosyphon (TPLT) with non-condensable gas (NCG) was attempted by fitting twin spiky ribbed twisted tapes (SRTTs) in the evaporator. The startup process and the steady-state boiling flow structures, boiling heat transfer rates, thermal resistance networks at various heater powers, and condenser thermal resistances were examined with 40% molar fraction of air in the TPLT. With treated water as the working fluid at an evaporator volumetric filling ratio of 50%, all tests were performed at subatmospheric pressures. The thermal performance improvement achieved by using SRTTs in the evaporator was determined by comparing the test results measured from the TPLT of the plain evaporator without NCG and the TPLT with NCG and SRTTs in the evaporator. Axial swirls generated in the evaporator suppressed the oscillatory interfacial structures caused by shooting intermittent vapor slugs, which led to improved boiling stability and reduced the overall thermal resistance. Correlations for evaluating the boiling Nusselt numbers over pool boiling, intermittent, and vapor regions as well as the dimensionless overall thermal resistance were devised for the present enhanced TPLT with NCG to represent all generated data.

I. INTRODUCTION

The vapor-liquid two-phase heat transfer loop has found various applications, such as the cooling of electronic chipsets and extraction of geothermal and solar energy. The thermal performance of this type of phase-change loop is conveniently evaluated as the overall thermal resistance (r_{th}); r_{th} is defined as the ratio between the heat source-to-sink temperature difference and the corresponding heat power transferred. By using a loop heat pipe (LHP), the capillary pressure generated in the wick was used to passively facilitate the circulation of the working fluid for transmitting heat by phase-change activities. The synthesis of Siedel et al., which listed all the relevant parameters affecting the performance levels of heat pipe loops, summarized some up-to-date steady-state models that resolved transport phenomena (Siedel et al., 2015). Many studies have investigated the influence of wick structure on the thermal performance levels of LHPs. A pore network model was proposed to study heat and mass transfer associated with phase change in a partially heated porous structure (Figus et al., 1999). Recently, a method was developed for optimizing the shapes of LHP capillary evaporator wicks (Nishikawara and Nagano, 2017). This study showed that a wick shape could be optimized by selecting a three-phase contact line (TPCL) of optimal length. The heat transfer rates in the evaporator initially increased with the TPCL length but then decreased as the TPCL length exceeded a critical value; this was attributable to large variations of the saturation temperature caused by the large pressure losses in grooved wicks. There is always a trade-off between the capillary forces generated by wicks and the accompanying complexities in thermal physics and manufacturing processes as well as the additional drags and thermal barriers caused by wicks in a vapor-liquid two-phase heat transfer device.

A two-phase loop thermosyphon (TPLT) without a wick was developed for long-distance heat transmission by using gravity for facilitating vapor–liquid circulation. The high phase-change heat-transfer rate between 10^3-10^5 W/m^{2}K in a typical TPLT (Vasiliev, 2005) permitted effective and efficient latent heat transmission with a small temperature difference between a heat source and a heat sink. In a TPLT operated at the specified temperature differences, the correlative relationship between mass and heat flows was of primary importance but was interdependently affected by various system parameters, including heat load, working fluid, driving and dragging forces, heat transfer rates in the evaporator and condenser, and geometrical features of the TPLT (Vasiliev, 2005). At the prescribed temperature difference between the evaporator, the differential saturation pressures are induced. The flow rate of vapor-liquid circulation in the TPLT was subject to the complex interdependent effects

Paper submitted 05/15/17; revised 07/13/17; accepted 11/06/17. Author for correspondence: Shyy Woei Chang (e-mail address: swchang@mail.ncku.edu.tw).
[1] Department of System and Naval Mechatronic Engineering, National Cheng Kung University, Tainan, Taiwan, R.O.C.
[2] Depart Department of System and Naval Mechatronic Engineering, National Cheng Kung University, Tainan, Taiwan, R.O.C.

caused by the boiling heat flux and condenser's thermal resistance ($r_{th,con}$) (Chang et al., 2012). because the flow rate of vapor-liquid circulation in the TPLT was subject to the complex interdependent effects caused by the boiling heat flux and condenser's thermal resistance ($r_{th,\mathrm{con}}$) (Chang et al., 2012). Because the local pressure decreases along a TPLT pathway were sensitive to local dryness factors, the loop-wise pressure distributions were interdependent with the enthalpy accountancy; this affected the thermodynamic states of the working fluid (Khodabandeh, 2005). Khodabandeh used a homogeneous model (Bowers and Mudawar, 1994) to predict the pressure drops along a tubular TPLT. Inherited from the homogeneous model with increased fluid density at elevated pressure, the frictional drags in a TPLT were inversely proportional to the homogeneous fluid density and were therefore decreased at increased pressures. This loop-wise accountancy of local pressure drops was of primary importance for predicting the thermal resistance network of a TPLT as the local fluid temperatures were affected by local fluid pressures and dryness factors during phase-change processes (Khodabandeh, 2005). Moreover, the phase-change heat-transfer rates also showed pressure dependency. The increased boiling heat transfer rates at elevated pressures were caused by the more active cavities at such pressures. Thus, an attempt to use threaded channels as evaporators in TPLTs with isobutane as the working fluid demonstrated improved boiling heat transfer rates at all tested pressures (Khodabandeh and Palm, 2002). Nevertheless, the boiling heat transfer rates in the evaporators of TPLTs at sub-atmospheric (Chang et al., 2012) and positive (Khodabandeh, 2005) pressures consistently agreed with Cooper's pool boiling correlation (Cooper, 1984). The static departure boiling theory (Niro and Baretta, 1990) suggests that the reduced departure of vapor bubbles at elevated pressures reduced the superheat required for bubble nucleation, thus activating smaller nucleation sites (Khodabandeh, 2005) to raise the boiling heat transfer rates; this agreed with the pressure contribution in Cooper's correlation (Cooper, 1984).

Another important phenomenon degrading the TPLT performance is the instability triggered by the phase-change activities that incurred various types of pressure and temperature fluctuations. Tadrist reviewed such types of two-phase instabilities for narrow channels and classified the boiling instabilities as static and dynamic modes (Tadrist, 2007). Static instabilities included flow excursion, interfacial transition of flow patterns, and boiling crises. The most common feature of dynamic instabilities was the density wave oscillation. With a single evaporator channel, the finite time lapse during bubble growth induced phase shifted between the entry flow and the pressure drops, thereby triggering self-sustained oscillations (Niro and Baretta, 1990). With an intermittent boiling regime characterized by a longer new bubble waiting time than the bubble growth time, the boiling instabilities acted as bulk stream pulsations (Kandlikar, 2002). With multiple evaporator channels, the upstream and downstream expansions of the vapor bubbles caused large amplitude fluctuations of the liquid-vapor interfaces that could lead to flow reversal in some evaporator channels of some TPLTs (Khodabandeh and Furberg, 2010).

The generation of non-condensable gas (NCG) is typically another important factor that can gradually deteriorate the thermal performance of a TPLT. Common NCGs such as nitrogen, light hydrocarbons, and carbon dioxide were produced by chemical reactions over an operational period (Randeep, 2010). Some NCG (mainly air) was absorbed in the construction material and diffused over time into the working fluid. NCG in a TPLT generally elevate the operating temperature, cause difficulties in startup, and degrade heat transmission in the evaporator and condenser. Such unfavorable NCG effects on the TPLT performance tend to be cumulative and irreversible. The present study aimed to solve the aforementioned problems.

Previous experiments with LHPs showed that NCGs mainly accumulated in the compensation chamber and led to an increase in the operating pressure and temperature (Randeep, 2010). As the increased partial pressure of NCG increased the operating pressure and corresponding saturation temperature during the startup period, the startup period was generally extended in the presence of NCGs. At 30 vol% NCG content, the startup time was 2.8 times greater than that in vacuum (Huang et al., 2016). At very low cooling duty, the presence of NCG even prevented the startup of the thermosyphon loop (He et al., 2013). For the steady-state operation of a TPLT with NCG, the evaporator temperature was increased, with an accompanying reduction in the overall thermal conductance (He et al., 2014). As the NCG coverage prevented direct phase-change activities at the condenser and evaporator walls, the thermal resistances of the condenser and evaporator were increased owing to the presence of the NCG layer. The unfavorable NCG effects became more significant with an increase in the NCG quantity (Brusly et al., 2013). The degradation of the thermal conductance was associated with the partial pressure of the NCG, which often led to an increase in heat leakage to the condenser but had a moderate influence on the evaporator conductance (Prado-Montes et al., 2014).

One method to reduce the thermal resistance of the NCG layer was to artificially boost turbulent activities by using a helical insert in a heat pipe or thermosyphon (Vasiliev et al., 2016). The swirling vapor flow induced in the evaporator by the centrifugal forces facilitated the separation of vapor from the liquid drops and ejected liquid droplets toward the evaporator walls. Along with such swirl-induced thermal performance improvements in the presence of NCG, turbulence could be increased by using an enhanced or ribbed helical insert (Vasiliev et al., 2016). In addition, the centrifugal forces induced by a helical insert improved the liquid-vapor segregation, thereby increasing vapor dryness up to 99% at the evaporator outlet and generating uniform wetting on the evaporator wall (Vasiliev et al., 2016). The improvement of vapor-liquid segregation in the thermosyphon upon using a helical insert caused a 30%-50% reduction in thermal resistance (Vasiliev et al., 2016).

In the present study, a spiky ribbed twisted tape (SRTT) was developed to integrate swirls for phase segregation and ribs for turbulence augmentation to moderate the impact of undesir-

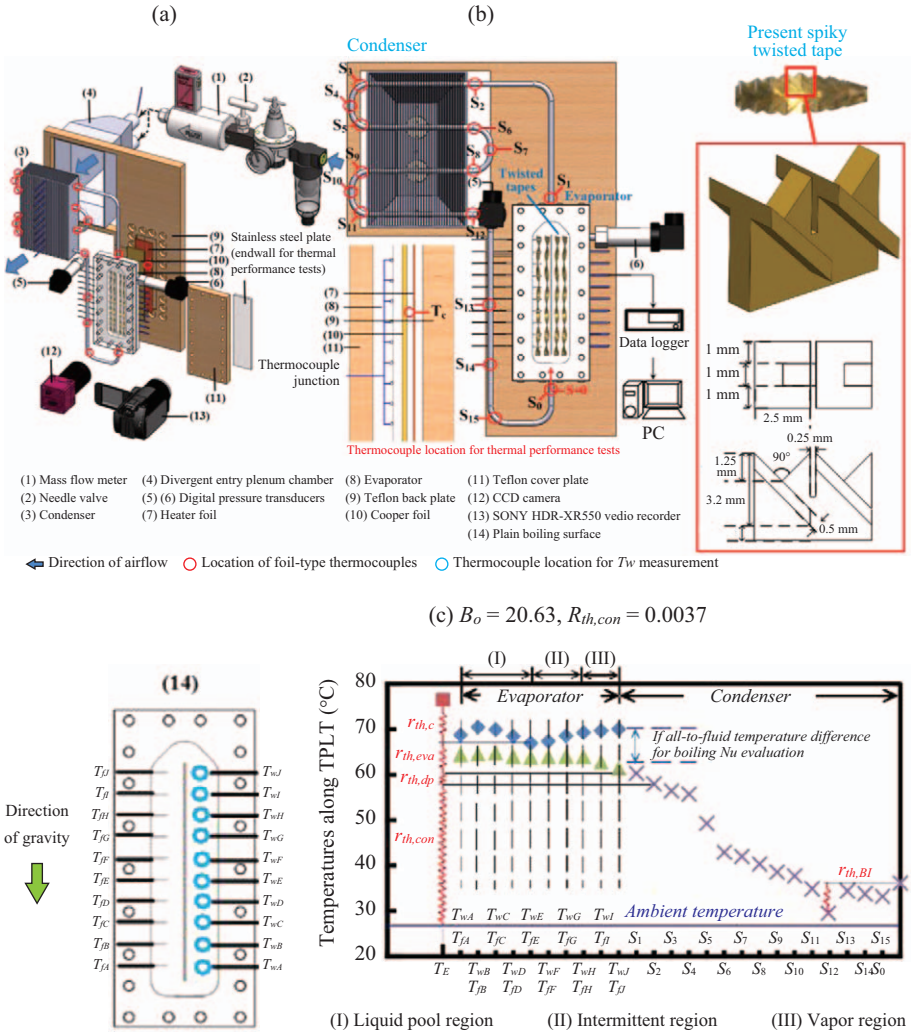

Fig. 1. (a) Thermosyphon loop, (b) spiky ribbed twist tape (SRTT), and (c) typical temperature variation along TPLT pathway, with definitions of constituent thermal resistances.

able NCGs. The test results obtained from the present TPLT with NCGs and SRTTs are compared with those obtained from a TPLT with a plain evaporator without NCGs (Chang et al., 2012) to clarify the thermal performance improvement caused by SRTT inserts. The selective test results for the present TPLT with SRTTs were acquired at 40% molar fraction of NCGs. With this NCG content, the overall thermal resistance showed a marginal decrease compared to that for the TPLT with a plain evaporator without NCGs (Chang et al., 2012). The boiling and condensation heat transfer rates and thermal resistance networks for the present TPLT with SRTTs with 40 vol% NCG were measured and the associated boiling flow structures were recorded. The test conditions involving various heating and cooling duties were respectively specified by the dimensionless boiling numbers (B_o) and condenser thermal resistance ($R_{th,\mathrm{con}}$). Along with the corresponding boiling flow images, the phase-change heat-transfer rates and thermal resistance properties at various B_o and $R_{th,\mathrm{con}}$ values were analyzed. A set of heat transfer correlations for evaluating the time-mean *Nu* over the evaporator and condenser and the dimensionless overall thermal resistances (R_{th}) using B_o and $R_{th,\mathrm{con}}$ as the controlling variables were devised to represent all the experimental data.

II. EXPERIMENTAL DETAILS

1. Test Facilities

The experimental facilities for the thermosyphon loop and the SRTT in the evaporator are shown in Figs. 1(a) and (b), respectively. The TPLT pipeline and tubular condenser with an extended cooling fin area of 585880 mm^2 were made of copper. The evaporator was made of a stainless steel plate, which provided sufficient stiffness to tighten the leakage-free glass endwall for flow visualization. The cooling airflow rate was adjusted to control the regional thermal resistance between the condenser and the surrounding ambience, which was referred to as the thermal resistance of the condenser ($r_{th,con}$), at the targeting test value. A mass flow meter (1) and needle valve (2)

were used to measure and adjust the air flow rate ($\dot{m}_a$) to the condenser (3) through a divergent entry plenum chamber (4). The air flow temperatures at the entry ($T_{a,i}$) and exit ($T_{a,o}$) of the cooling chamber with a fin array were measured using K-type thermocouples. The condenser cooling power at each test condition was evaluated as $\dot{m}_a Cp_a(T_{a,o}\text{-}T_{a,i})$, and the thermal resistance of the condenser ($r_{th,con}$), as defined by Eq. (1), was controlled at the targeted values by varying $\dot{m}_a$ to accommodate the various entry temperatures of the condenser ($T_{f,con}$) at different values of heater power or $T_{a,i}$ or both.

$$r_{th,con} = (T_{f,con} - T_{a,i}) / [\dot{m}_a Cp_a (T_{a,o} - T_{a,i})] \quad (1)$$

With the entire pipeline and evaporator wrapped in thermal insulation material to reduce external heat loss, the cooling power of the condenser, evaluated as $\dot{m}_a Cp_a(T_{a,o}\text{-}T_{a,i})$, was close to the heater power (Q) supplied to the evaporator. The differences between the condenser cooling power and Q were less than 8%. Pressure transducers (5) and (6) respectively detected the operating pressures of the evaporator and condenser. To generate a basically uniform heat flux, an electrical heater foil (7) with effective heating area of 140 × 40 mm^2 was attached on the back wall of the evaporator (8).

The evaporator (8) was constructed by two rectangular channels with dimensions of 138 × 20 × 10 mm^3 each, providing a channel width-to-height ratio (aspect ratio, AR) of 2 and hydrodynamic diameter (d) of 13.5 mm. The TPLT was filled with distilled and deionized water until the water level reached the mid-span of the evaporator channel, giving a 50% volumetric filling ratio. To realize a 40% molar fraction of air (NCG) in the present thermosyphon loop, a vacuum process was performed by immersing the entire thermosyphon loop in an ice water bath at 0°C. With the thermosyphon loop filled with treated water, the evacuation process stopped at absolute pressure of 1016 Pa. At the equilibrium condition, the partial pressure of water-vapor in the present TPLT corresponded to the saturated pressure of water-vapor at 0°C, 611.2 Pa. Referring to the Delton model, the partial pressure of air (NCG) was 404.8 Pa. Thus, the molar fraction of air can be determined from the pressure ratio of 404.8/1016 as 40%. All experiments were performed with a 40% molar fraction of air (NCG) in the present thermosyphon loop.

The discharge port of the evaporator was connected with a vertical tube of inner diameter 4 mm so that the abrupt ratio at the evaporator exit was 2843. Owing to the momentum change of the saturated or wet steam through this type of abrupt flow exit and the downstream elbow bend in front of the condenser, the pressure drop from the evaporator exit to the condenser entry resulted in a noticeable temperature drop, thus generating the so-called pressure drop thermal resistance ($r_{th,dP}$), which is defined as the ratio of the temperature drop from evaporator exit to condenser inlet ($\Delta T_{,dP}$) to the heater power.

The heater foil (7) was squeezed between the 30-mm-thick Teflon back plates (9) and the 0.5-mm-thick copper foil (10) to spread the heat flux over the evaporator back wall. The front endwalls of the evaporator (8) were made of 5-mm-thick stainless steel plate and 20-mm-thick glass plate inlaid in the 25-mm-thick Teflon frame (11) for thermal performance and flow visualization tests, respectively. The evaporator assemblies were tightened using axial bolts with O-rings and a high-temperature sealant to prevent leakage. The boiling flow structures in the evaporator were recorded by the CCD system (12) at 300 fps. A SONY HDR-XR550 video recorder (13) was used to synchronously record the boiling flow structures and temporal variations of the evaporator wall temperatures. In the present study, the steady state was assumed to have been reached when several successive time-averaged wall temperature scans from the evaporator were less than 0.3K; 45-80 min were generally required to satisfy the steady-state condition after Q or $r_{th,con}$ was adjusted.

To measure the boiling heat transfer rates with minimum disturbances on the flow field, 10 K-type thermocouples were installed such that they penetrated the cores of another evaporator channel at axial locations corresponding to the measurement locations for wall temperature along the adjacent evaporator channel. Along the thermosyphon loop, K-type thermocouples were installed at the locations shown in Fig. 1(a) to calculate the regional thermal resistances that composed the total thermal resistance (r_{th}). All K-type thermocouple signals were transmitted to the computer through a Fluke NetDAQ data logger that provided 0.01 K precision for temperature measurements.

The thermal resistance of the condenser ($r_{th,con}$) was treated as a controlling parameter for adjustment of the test conditions during experiments. The overall thermal resistance of the present TPLT (r_{th}) comprised the contact thermal resistance between the evaporator and the heater ($r_{th,c}$), evaporator thermal resistance ($r_{th,eva}$), pressure drop thermal resistance ($r_{th,dP}$), and condenser thermal resistance ($r_{th,con}$) in series. As the boiling instabilities in the evaporator channel triggered liquid surface oscillations to incur backward hot flow into the condenser, the entry fluid temperature of the evaporator was increased, which caused T_E elevation, leading to an increase in the total thermal resistance (r_{th}). The thermal resistance due to boiling instability ($r_{th,BI}$) was therefore implicitly inclusive in $r_{th,con}$. To typify the composition of these constituent thermal resistances along the thermosyphon loop, the temperature variation along the TPLT pathway at B_o = 20.63 and $R_{th,con}$ = 0.0037 is shown in Fig. 1(c). Referring to the locations at which the temperatures were measured along the present thermosyphon loop, as shown in Fig. 1(c), r_{th}, $r_{th,c}$, $r_{th,eva}$, $r_{th,dP}$, $r_{th,con}$, and $r_{th,BI}$ are respectively defined as follows.

$$r_{th} = (T_E - T_{a,i}) / Q \quad (2)$$

$$r_{th,c} = (T_E - T_{w,eva}) / Q \quad (3)$$

$$r_{th,eva} = (T_{w,eva} - T_{f,eva}) / Q \quad (4)$$

$$r_{th,dP} = (T_{f,eva} - T_{f,con}) / Q \quad (5)$$

$$r_{th,con} = (T_{f,con} - T_{a,i})/Q \quad (6)$$

$$r_{th,BI} = (T_{f,con}\big|_{exit} - T_{f,eva}\big|_{extry})/Q \quad (7)$$

In these equations, T_E is the temperature at the center of the electrical heater (7), and $T_{f,con}\big|_{exit}$ and $T_{f,eva}\big|_{extry}$ are respectively the fluid temperatures at the exit of the condenser and the entrance of the evaporator. The contact thermal resistance ($r_{th,c}$) remained unchanged, whereas all other constituent thermal resistances changed when B_o or $R_{th,con}$ were adjusted. The wall-to-fluid temperature differences measured from the evaporator channels with the present twin SRTTs were selected to calculate the local boiling heat transfer coefficients (h) and boiling Nusselt number (Nu) along the evaporator channel.

As shown in Fig. 1(b), the stainless steel SRTT in the evaporator was 1 mm thick, 10 mm wide, and 138 mm long. Spiral ribbed spikes emanated along the central helix on the SRTT surfaces. The twist ratio (y) was defined as the ratio of the twist pitch (Pi) to the tape width (W_T), and it was found to be 3.5. Each spike was 1 mm wide; the number of spikes for each twist pitch was 11. A V-cut at each spike tip was machined, and near-wall bursting flow was induced through it. While the ribs and spikes augmented turbulent activities in general, the use of regular triangular V-cuts with side length of 1.8 mm on the edge of each spike for the present SRTT assisted in forming an additional pathway for liquid refilling upon vapor departure from the evaporator wall. For boosting turbulent activities in the axial swirls, two skewed broken ribs of $4.5 \times 0.5 \times 1$ mm^3 with an attack angle of 45° to the spike centerline were machined on two sides of each spike. In each evaporator channel, two identical SRTTs with the same twist orientation were installed. The axial swirls induced by the present SRTTs acting with amplified turbulence were intended to suppress the NCG effects (Vasiliev et al., 2016).

2. Test Program and Data Reduction

The test conditions specified included the boiling number (B_o) and dimensionless thermal resistance of condenser ($R_{th,con}$). B_o was varied by adjusting the heater power to 80, 100, 120, 140, 150, and 180 W. At each fixed boiling number, thermal performance measurements were performed at four $R_{th,con}$ values of 0.25, 0.3, 0.35, and 0.4, by adjusting the airflow rates through the fin assembly of the condenser. Flow visualization tests were performed individually at identical Bo and $R_{th,con}$ selected for thermal performance tests.

For calculating B_o, thermal resistances, and boiling and condensation heat transfer rates, the net thermal power transferred into the evaporator was determined by subtracting the heat loss from the total power supplied by the heater. To determine the heat loss characteristics, a set of calibration heat loss tests was performed. The heat loss correlation obtained from the heat loss tests was incorporated into a data processing program for calculating the heat transfer rates and thermal resistances. Owing to the use of thermal insulation material to reduce external heat loss, the present heat loss flux was less than 6% of the total heat flux supplied. By using the convective heat flux (q) determined by subtracting the heat loss flux from the supplied heat flux, the local boiling heat transfer rate (h) was defined as

$$h = q/T_w - T_f \quad (8)$$

where T_w and T_f are the measured evaporator-wall temperatures and corresponding fluid temperatures, respectively. To determine the temperature at the inner wall of the evaporator (T_w), the one-dimensional Fourier conduction law was adopted to correct the thermocouple data to the inner wall temperatures based on local q.

The nondimensional presentations of thermal performance levels for the present TPLT in terms of the Nusselt number (Nu) and dimensionless thermal resistance (R_{th}) were expressed as functions of Bo and $R_{th,\mathrm{con}}$ in Eq. (9).

$$Nu \text{ or } R_{th} = \Psi\left\{B_o, R_{th,con}, \text{boundary conditions}\right\} \quad (9)$$

where the boiling number (B_o), Nusselt number (Nu), and dimensionless thermal resistance (R_{th}) are defined as

$$B_o = QC_{pL}/(h_{fg}k_L d) \quad (10)$$

$$Nu = hd/k_L \quad (11)$$

$$R_{th} = r_{th}k_L d \quad (12)$$

h_{fg} and k_L in Eqs. (10)-(12) respectively denote the latent heat and thermal conductivity of water at the measured evaporator pressure (P_E). The h_{fg}, k_L, and C_{pL} values were evaluated at P_E. The non-dimensional expression of P_E, P^*, was defined as the ratio of P_E to P_{cr}, where P_{cr} is the critical pressure of the working fluid. Eq. (9) with its functional structure of Ψ was devised from a parametric analysis through which the isolated and interdependent B_o and $R_{th,con}$ impacts on Nu and R_{th} were obtained.

The experimental uncertainties were analyzed to approximate the precision errors in the measurement of parameters following the ASME *J. Heat Transfer* policy for reporting experimental uncertainties (ASME Editorial, 1993). The experimental uncertainties of the controlling variables, including B_o, $R_{th,con}$, and P^*, were calculated from the precision errors of all constituent parameters such as h_{fg}, k_L, and C_{pL}. The reductions in the experimental uncertainties for the dimensionless parameters were achieved by minimizing the precision error of each measuring device. With the respective precision errors for temperature and pressure measurements of 0.01 K and 10 Nm^{-2}, the maximum precision errors for h_{fg}, k_L, and C_{pL} were 1.6%, 1.5%, and 1.2%, respectively. The maximum uncertainty for the wattmeter was 1.7%; the estimated uncertainties of the derived para-

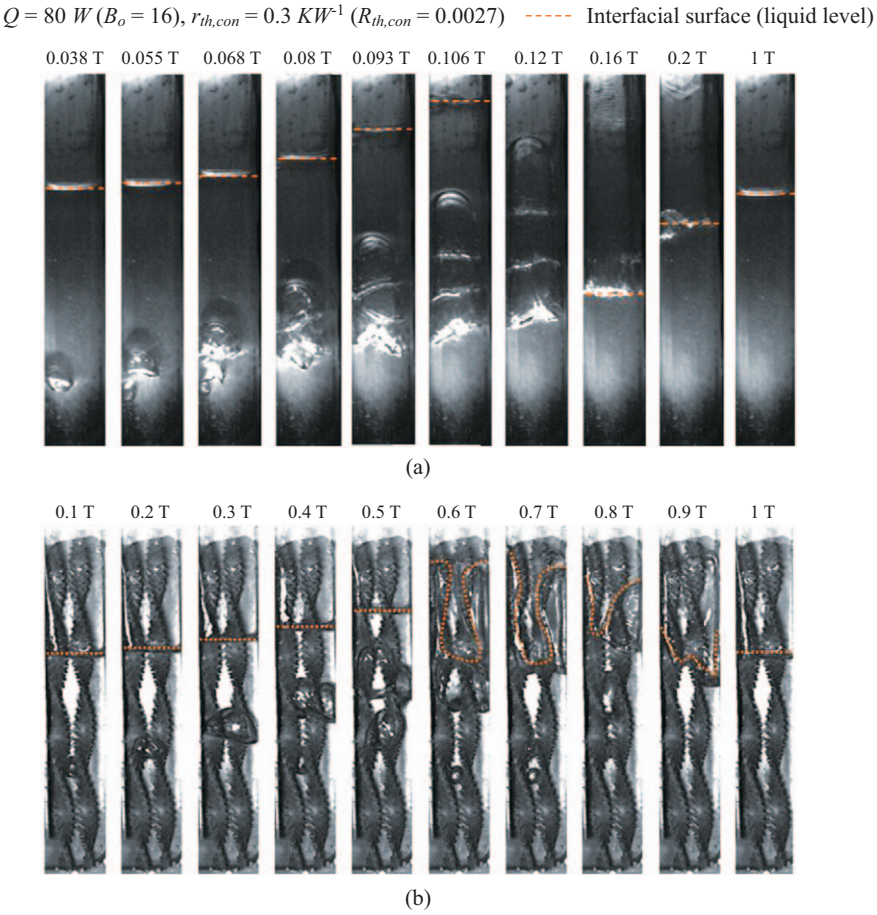

Fig. 2. Sequential boiling flow snapshots at intermitted flow regimes in (a) plain evaporator without NCG (Chang et al., 2012) (b) evaporator channel with twin SRTTs and 40 vol% NCG.

meters for heat flux (q) and thermal resistance (r_{th}) were 3.8% and 6.8%, respectively. The maximum uncertainties for B_o, R_{th}, Nu, and P^* were approximately 6.99%, 5.85%, 9.6%, and 9.8%, respectively.

III. RESULTS AND DISCUSSION

1. Boiling Flow Structures

Fig. 2 shows a comparison of the differential boiling flow structures in the (a) plain evaporator without NCG (Chang et al., 2012) and (b) present evaporator channel with twin SRTTs and 40 vol% NCG. For both TPLTs with and without SRTT/NCG, the boiling flow structure at low heater power started from the intermittent boiling regime, in which a tiny vapor bubble was initiated from a nucleation site with subsequent growth on the evaporator wall prior to bubble departure. Once the volumetric buoyancy force overcame the surface tension, the vapor bubble drifted away from the nucleation site and kept expanding during its upward journey along the evaporator channel, as shown in Figs. 2(a) and (b). Nevertheless, the oscillations of the vapor-liquid interface caused by the upward drifts of the intermittent vapor bubbles along the evaporator channels with and without SRTT are different, as shown in Fig. 2. In the plain evaporator channel (Chang et al., 2012), the expansion of the intermittent vapor bubble caused the formation of a typical Taylor bubble to uplift the liquid level until the Taylor bubble erupted. Once the Taylor bubble erupted in the plain evaporator channel without NCG, the liquid level oscillated, as shown in Fig. 2(a). The amplitudes of such liquid level oscillations in the plain evaporator channel without NCG were mainly determined by the length of the Taylor bubble before its eruption (Chang et al., 2012). When the liquid level in the evaporator channel moved downward to push the hot liquid from the evaporator into the condenser, the backwash hot flow preheated the subcooled condensate in the condenser, leading to the so-called boiling instability thermal resistance indexed by the temperature difference between the condenser exit and the evaporator entry.

With the present twin SRTTs in an evaporator channel, the expansion and eruption of an intermittent vapor bubble were affected by swirls and spirally arranged spikes, even when NCG was present. As demonstrated by the sequential boiling flow snapshots of the present evaporator channel with twin SRTTs, as shown in Fig. 2(b), the drifting process of the Taylor bubble was affected by the axial swirls and helically arranged spikes

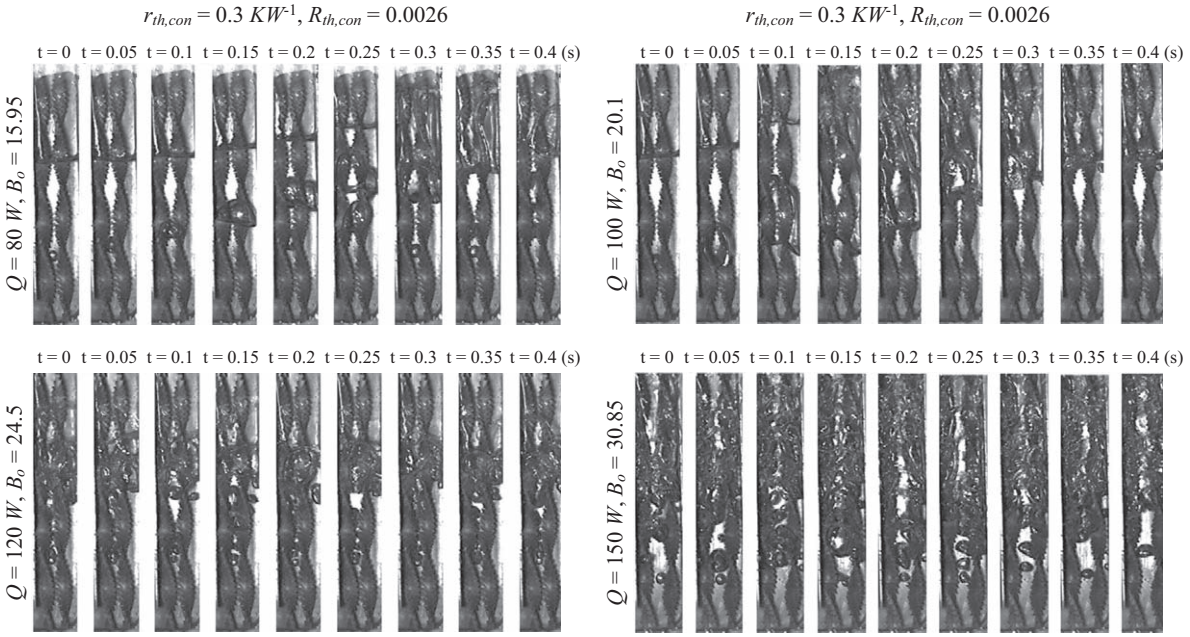

Fig. 3. Sequential flow snapshots with four ascending heater powers at fixed $r_{th,con}$ of 0.3 kW^{-1}.

with ribs and V-cuts. In this regard, the intermittent vapor slugs were considerably distorted during their upward journey from the liquid pool to the vapor dome along the evaporator channel with twin SRTTs. A vapor slug initiated from the nucleation site in the liquid pool of the evaporator channel with twin SRTTs was subject to a twist action during its uplift expanding process. With the present twin SRTTs at 0.6 intermittent periods (0.6T), the burst of the vapor slug through the interfacial surface led to two up-surging liquid streams along the two channel sidewalls with subsequent liquid falls to recover the liquid level at 1 T, as shown in Fig. 2(b). However, in the plain evaporator channel without NCG, the eruption of the Taylor bubble through the interfacial surface kept elevating the liquid level until the entire Taylor bubble passed through the evaporator exit to form a subsequent liquid level as the trailing edge of the Taylor bubble; this caused a considerable drop in the liquid level, as shown in Fig. 2(a). The displacements of the liquid level in the plain channel without NCG were considerably larger than those in the present evaporator channel with twin SRTTs and NCG, as indicated by the comparison of Figs. 2(a) and (b). The extent of oscillation of the liquid level in the present evaporator channel with twin SRTTs and NCG was considerably lower than the oscillation in the plain evaporator channel without NCG, as shown in Fig. 2. Owing to the moderated backwash hot flow into the condenser with the suppressed preheating effect on the entry fluid of the evaporator using the present twin SRTTs, the thermal resistance attributed to the boiling instability for the present TPLT with SRTTs was reduced relative to that for the TPLT with the plain evaporator channel. However, the typical shape of the Taylor bubble formed in a plain evaporator channel in the intermittent boiling flow regime could not be generated in the present evaporator channel with twin SRTTs, as shown in Fig. 2. Nevertheless, as in the boiling flow structures affected by boiling heat flux and operating pressures in the plain evaporator channel (Chang et al., 2012), various boiling flow regimes emerged at different heating or cooling duties for the present TPLT with SRTTs and NCG. The effects of Q (B_o) and $r_{th,con}$ ($R_{th,con}$) on the boiling flow structures in the present evaporator channel with twin SRTTs and NCG are respectively shown in Figs. 3 and 4, in which the flow snapshots taken at fixed Q (B_o) or $r_{th,con}$ ($R_{th,con}$) with various $r_{th,con}$ ($R_{th,con}$) and Q (B_o) are compared.

The sequential boiling flow snapshots at four ascending heater powers (Q) with fixed $r_{th,\mathrm{con}}$ of 0.3 kW^{-1} are shown in Fig. 3 to demonstrate the impact of Q on boiling flow structures in the evaporator channel with twin SRTTs and NCG. It is worth noting that the $r_{th,\mathrm{con}}$ definition of $(T_{f,\mathrm{con}} - T_{a,i})/Q$ requires the responsive increase of $(T_{f,\mathrm{con}} - T_{a,i})$ to match the increase of Q for maintaining $r_{th,\mathrm{con}}$ ($R_{th,\mathrm{con}}$) at a fixed value. As $T_{a,i}$ is close to ambient temperature, the vapor temperature entering the condenser ($T_{f,\mathrm{con}}$) increases as Q increases when $r_{th,\mathrm{con}}$ is fixed. Thus, the evaporator pressures and boiling wall superheats are correspondingly elevated as Q increases at fixed $r_{th,\mathrm{con}}$. In Fig. 3, at Q = 80 W and $r_{th,\mathrm{con}}$ = 0.3 kW^{-1}, the boiling flow structures show an intermittent pattern, and the bursting of vapor slugs through the interfacial surface emerges at t = 0.3 s. As Q increases from 80 to 100 W, the bursting of the vapor slug through the interfacial surface advances to t = 0.15 s, while the boiling activities still remain in the intermittent regime. With a further increase of Q to 120 W, the boiling activities transition to the continuous mode, and the size of vapor bubbles shrinks noticeably relative to that observed in the intermittent boiling regime. At Q = 150 W, the continuous boiling activities in the liquid pool are intensified with coherent vapor bubbles

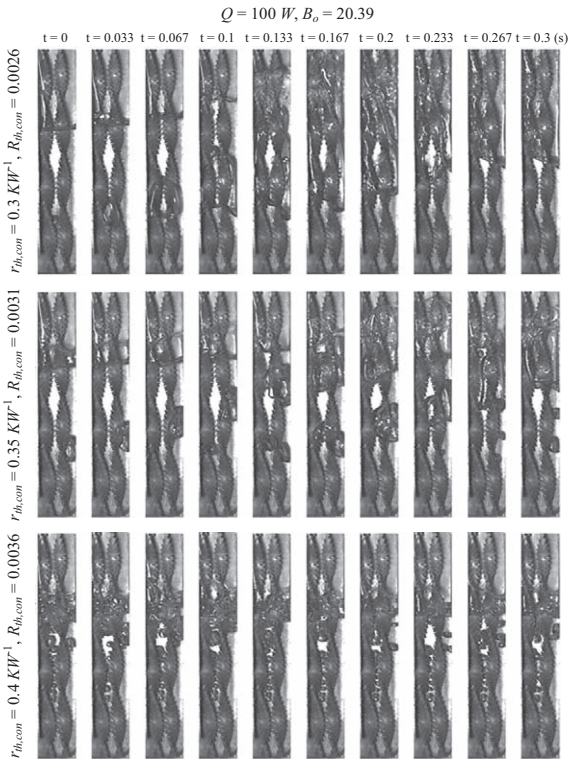

Fig. 4. Consecutive snapshots of boiling flow images at Q = 101.55 W and $r_{th,con}$ = 0.3, 0.35, and 0.4 kW^{-1}.

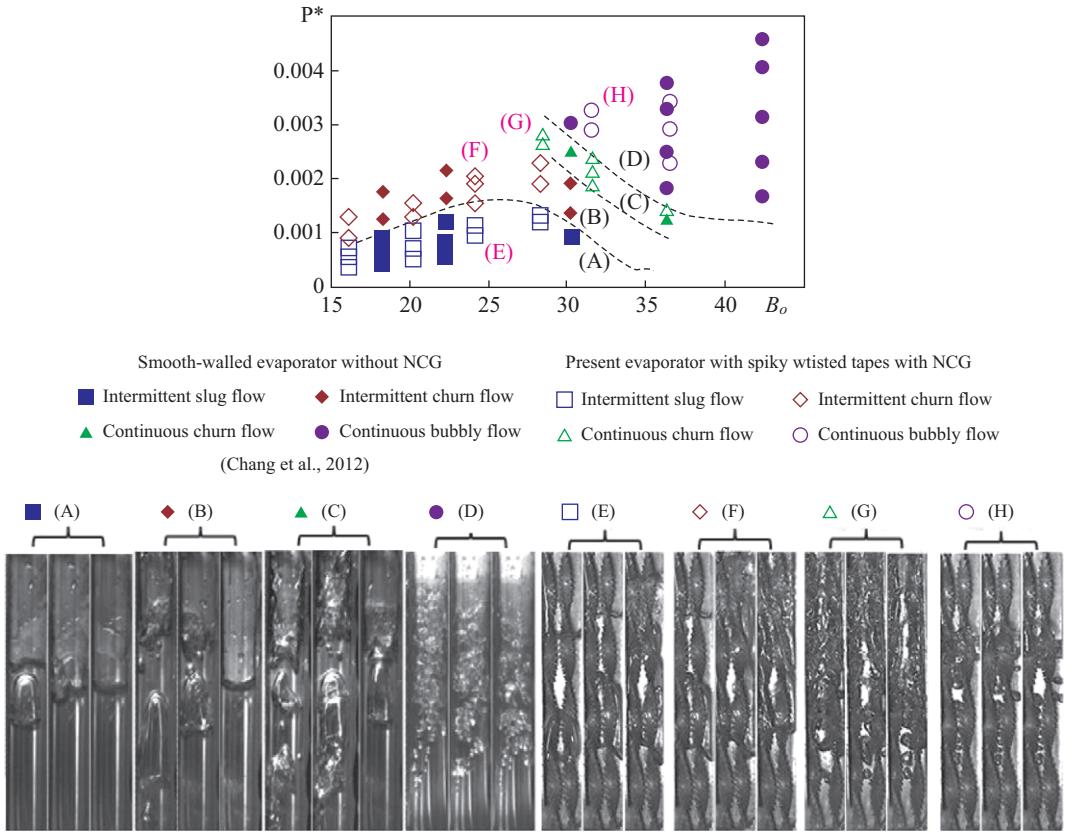

Fig. 5. Boiling regime specified by P^* and B_o for plain evaporator without NCG (Chang et al., 2012) and enhanced evaporator channel with twin SRTTs with 40 vol% NCG.

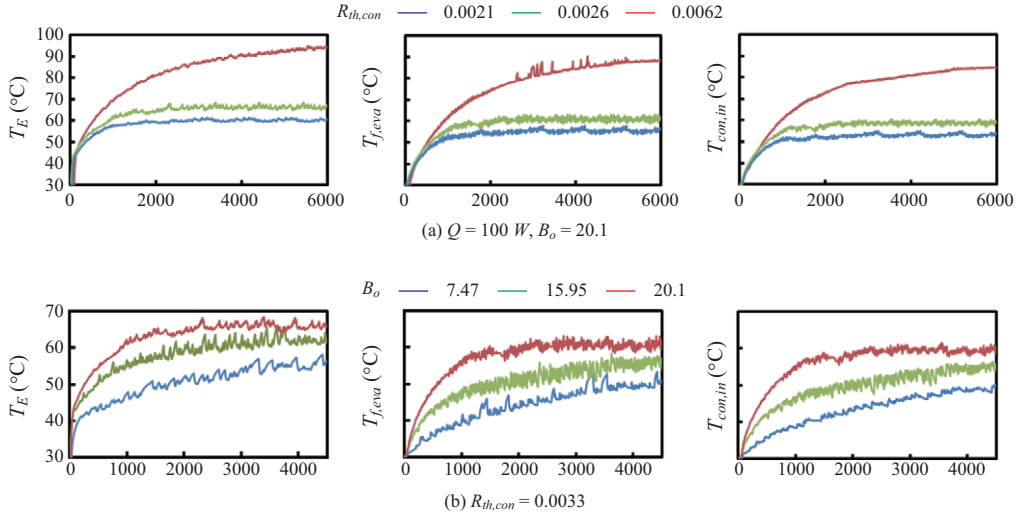

Fig. 6. Transient variations of T_E, $T_{f,eva}$, and $T_{con,in}$ during the startup period of TPLT at (a) Q = 100 W, $R_{th,con}$ = 0.0021, 0.0026, and 0.0062 and (b) $R_{th,con}$ = 0.0033, B_o = 7.47, 15.95, and 20.1.

occupying the entire vapor dome in the evaporator channel with twin SRTTs. The variations of the boiling flow structures revealed by Fig. 3 mainly reflect the impacts of increasing evaporator superheat and pressure as Q increases at fixed $r_{th,con}$; this consequently affects the boiling heat transfer rate and overall thermal resistance of the present TPLT, as demonstrated later.

With fixed Q, $r_{th,con}$ is increased by increasing $(T_{f,con} - T_{a,i})$ by using a reduced cooling airflow rate through the condenser. The condenser pressure is accordingly increased, and the fluid temperature entering the evaporator is consequently increased. Fig. 4 shows the modifications of the boiling flow structures in consecutive snapshots as $r_{th,con}$ increases from 0.3 → 0.35 → 0.4 kW^{-1} at fixed Q of 101.55 W. At $r_{th,con}$ = 0.3 kW^{-1}, the tiny vapor bubbles detaching from the nucleation sites keep expanding to form intermittent vapor slugs that are disrupted after around 0.167 s, and transition into two streams of upsurging liquid film along two channel sidewalls. As $r_{th,con}$ increases from 0.3 to 0.35 kW^{-1}, the growing rates of vapor bubbles from the nucleation sites along their upward voyages are suppressed, while the boiling activities still remain intermittent. At $r_{h,con}$ = 0.35 kW^{-1}, the formation of large vapor slugs observed at $r_{th,con}$ = 0.3 kW^{-1} is noticeably suppressed as a result of increased P* owing to an increase in $r_{th,con}$. With a further increase of $r_{th,con}$ from 0.35 to 0.4 kW^{-1}, the sizes of the vapor bubbles continuously decrease and the boiling activities transition to a continuous nucleate boiling regime, as shown in Fig. 4.

Regardless of the interfacial modes of the boiling activities that emerged at different Q and $r_{th,con}$, three distinct flow regions with different heat transfer properties, namely, the region of liquid pool with vapor bubbles, intermittent flow region subject to free-surface oscillations, and vapor region are sequentially developed from the evaporator entry toward its exit. The flow map of the boiling regime specified by P^* and B_o for the present TPLT with SRTTs and NCG and the TPLT of the plain evaporator without NCG (Chang et al., 2012) are compared in Fig. 5.

As shown in Figs. 2 and 3, the variation of the boiling flow regime in the present evaporator channel with SRTTs and NCG caused by increasing B_o or decreasing $R_{th,con}$ with accompanying P^* variation follows the trail from intermittent slug flow → intermittent churn flow → continuous churn flow → continuous bubbly flow. From the comparison in Fig. 5, the differential vapor shapes at various boiling flow regimes in the evaporator channels without and with SRTTs are evident. Except for the continuous nucleate boiling regime, the shapes of vapor bubbles in the present evaporator channel with SRTTs are highly skewed or twisted in comparison with those seen in the plain evaporator channel, as shown in Fig. 5. However, the interfacial boundaries segregating the different boiling flow regimes for the evaporator channels without (Chang et al., 2012) and with twin SRTTs are similarly seen in Fig. 5. As our previous work (Chang and Lin, 2013) revealed the different segregation interfacial boundaries in the flow map between the TPLTs with smooth and scale roughened evaporator walls, the similar interfacial boundaries between the TPLTs with and without (Chang et al., 2012) SRTTs shown in Fig. 5 suggest that the segregation interfacial boundaries in a flow map are dominated by the roughness of the boiling surface rather than by the retrofits.

2. Thermal Performance Levels

1) Startup Performance

Initially, the startup performance of the present TPLT with SRTTs and NCG is examined by analyzing the transient T_E, $T_{f,eva}$, and $T_{con,in}$ responses to the variations of $R_{th,con}$ (Q) at fixed Q ($R_{th,con}$) during the startup periods at (a) Q = 100 W, $R_{th,con}$ = 0.0021, 0.0026, and 0.0062 and (b) $R_{th,con}$ = 0.0033, B_o = 7.47, 15.95, and 20.1, as shown in Fig. 6.

As shown in Fig. 6, all transient T_E, $T_{f,eva}$, and $T_{con,in}$ variations during the startup period follow the typical pattern of exponential increase toward steady-state levels. With NCG in the

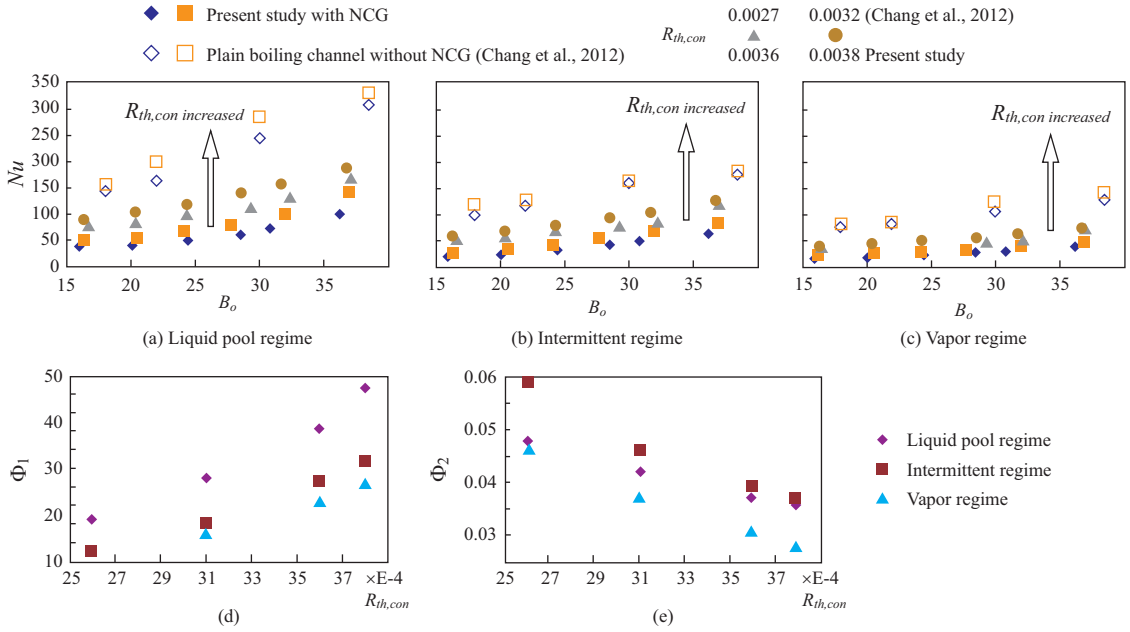

Fig. 7. Regionally averaged *Nu*: (a) liquid pool, (b) intermittent, (c) vapor regimes at various B_o with fixed $R_{th,con}$, (d) Φ_1, and (e) Φ_2 variations against $R_{th,con}$ for three flow regimes.

present TPLT enhanced by SRTTs, the temporal $T_{f,eva}$ oscillations shown in Fig. 6 trigger corresponding T_E and $T_{con,in}$ oscillations. The thermal inertial constructed by the present evaporator wall and the viscous dissipations of wet steam through the pipeline between the evaporator and the condenser damps out the oscillating amplitudes of T_E and $T_{con,in}$ from the $T_{f,eva}$ counterparts, as shown in Fig. 6. Following the temporal amplifications of $T_{f,eva}$ oscillations as t increases, the oscillating amplitudes of T_E and $T_{con,in}$ accordingly increase owing to the corresponding evolution of the boiling flow structures in the present evaporator channel, as shown in Fig. 6. In Fig. 6(a), at fixed $Q = 100$ W with three ascending $R_{th,con}$, the startup period is systematically extended as $R_{th,con}$ increases. However, as Q increases at fixed $R_{th,con}$, the startup period is reduced, as shown in Fig. 6(b). Among the three comparative cases with identical $R_{th,con}$ of 0.0033 shown in Fig. 6(b), the larger amplitudes of T_E, $T_{f,eva}$, and $T_{con,in}$ oscillations emerge at $B_o = 15.95$ owing to the transition of the boiling flow from intermittent slug to intermittent churn.

2) Boiling Heat Transfer

Based on the response to different types of boiling activities along the present evaporator channel with SRTTs, three heat transfer regions are identified: (1) liquid pool region, (2) intermittent region with oscillating free surface, and (3) vapor region. The Local Nusselt numbers measured from three heat transfer regions along the evaporator channel are averaged and the impacts of B_o or $R_{th,con}$ on the regional heat transfer properties are examined. Fig. 7 shows the variations of the regionally averaged Nusselt number (Nu) over the three evaporator regions at various B_o or $R_{th,con}$. The Nu values over the three evaporator regions with six ascending B_o at $R_{th,con} = 0.0027$, 0.0032, 0.0036, or 0.0038 are respectively shown in Figs. 7(a)-(c).

For each flow region in the present evaporator channel with SRTTs and NCG, the regionally averaged Nu increases as B_o or $R_{th,con}$ increases to reflect the increased superheat over the boiling surface and the corresponding variations in boiling flow structures. As shown in Figs. (2)-(4), the increase in B_o or $R_{th,con}$ induces the transition of the boiling flow regime from intermittent slug/churn toward continuous nucleate boiling. As the boiling heat transfer rates in the continuous nucleate boiling regime are higher than those developed in the intermittent slug/churn flow regimes owing to the lower vapor coverage on the boiling wall with higher rate of liquid replenishment, the Nu over the liquid pool, intermittent, and vapor regions consistently increases as B_o or $R_{th,con}$ increases, as shown in Fig. 7. A comparison of the Nu levels obtained with the identical set of B_o and $R_{th,con}$ between the three flow regions along the present evaporator channel with twin SRTTs indicates that the highest Nu consistently emerges over the liquid pool region, followed by the intermittent and vapor regions.

To find the Nu correlations for the three flow regions along the present evaporator channel, the consistent B_o-driven Nu data trends shown in Figs. 7(a)-(c) enable each Nu correlation to be expressed in the following general form:

$$Nu = \Phi_1\left\{R_{th,con}\right\} \times \exp\left[\Phi_2\left\{R_{th,con}\right\} \times B_o\right] \qquad (13)$$

In Eq. (13), the correlative Φ_1 and Φ_2 values over the liquid pool, intermittent, and vapor regions are functions of $R_{th,con}$. The variations of Φ_1 and Φ_2 against $R_{th,con}$ for the liquid pool, intermittent, and vapor regions are respectively shown by Figs. 7(d) and (e). Following the Φ_1 and Φ_2 varying trends shown in

Figs. 7(d) and (e), the Φ_1 and Φ_2 values expressed as functions of $R_{th,con}$ are represented by Eqs. (14)-(16) and (17)-(19) for the liquid pool, intermittent, and vapor regions, respectively.

$$\Phi_1 = 13389E5 \times R_{th,con}^{\ 3.068} \quad \text{liquid pool region} \tag{14}$$

$$\Phi_1 = 37773E6 \times R_{th,con}^{\ 3.748} \quad \text{intermittent region} \tag{15}$$

$$\Phi_1 = 45685E5 \times R_{th,con}^{\ 3.409} \quad \text{vapor region} \tag{16}$$

$$\Phi_2 = 0.099 - 25.91 \times R_{th,con} + 2450.6 \times R_{th,con}^{\ 2} \quad \text{liquid pool region} \tag{17}$$

$$\Phi_2 = 0.209 - 85.39 \times R_{th,con} + 10514 \times R_{th,con}^{\ 2} \quad \text{intermittent region} \tag{18}$$

$$\Phi_2 = 0.117 - 35.36 \times R_{th,con} + 3139.3 \times R_{th,con}^{\ 2} \quad \text{vapor region} \tag{19}$$

A comparison of all experimental *Nu* data with the correlation results obtained using Eqs. (13)-(19) reveals a maximum discrepancy of ±21%. Based on the favorable agreement between the experimental *Nu* data and the correlation results, Eqs. (13)-(19) can be used for evaluating the regionally averaged heat transfer levels in the present evaporator channel with twin SRTTs and 40 vol% NCG. Figs. 7(a)-(c) also show a comparison of compatible *Nu* data measured from the similar TPLT with plain evaporator channels without NCG (Chang et al., 2012). Owing to the presence of 40 vol% NCG in the present TPLT with SRTTs, the boiling *Nu* over the liquid pool, intermittent, and vapor regions in the present evaporator channel is consistently less than that in the plain channel TPLT without NCG (Chang et al., 2012).

3) Thermal Resistance

As shown in Fig. 1(c), the constituent thermal resistances of $R_{th,c}$, $R_{th,eva}$, $R_{th,dP}$, $R_{th,con}$, and $R_{th,BI}$ for the total thermal resistance (R_{th}) are defined by the regional temperature drops along the present thermosyphon loop. The thermal resistance attributed to the boiling instability ($R_{th,BI}$) is implicitly inclusive in $R_{th,con}$. By adjusting B_o or $R_{th,con}$ to vary the boiling activities in the evaporator or the pressure and subcooling condition in the condenser, the composition of these regional thermal resistances as well as the total thermal resistance (R_{th}) are accordingly changed; however, the contact thermal resistance is basically invariant, being around 0.05 kW^{-1}. In this regard, the total thermal resistance decreases as B_o increases but increases as $R_{th,con}$ increases, as demonstrated later. The percentages of the constituent thermal resistances in R_{th} are also affected by the responsive R_{th} variations caused by varying B_o or $R_{th,con}$. Thus, the percentage of contact thermal resistance ($R_{th,c}$) in R_{th} is altered by varying B_o

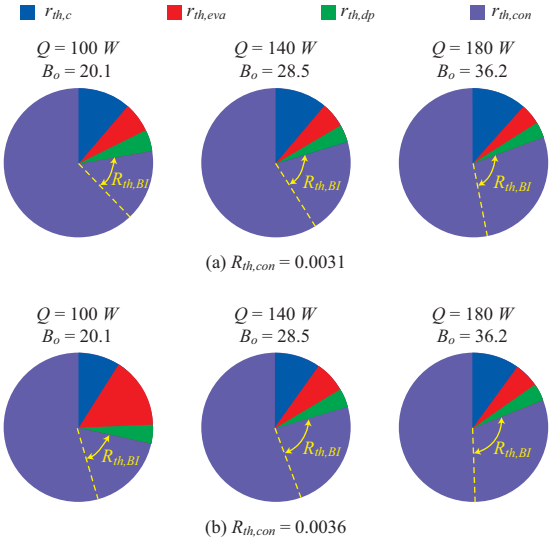

Fig. 8. Variations of composition of constituent thermal resistances for R_{th} by varying Q (B_o) at fixed $R_{th,con}$.

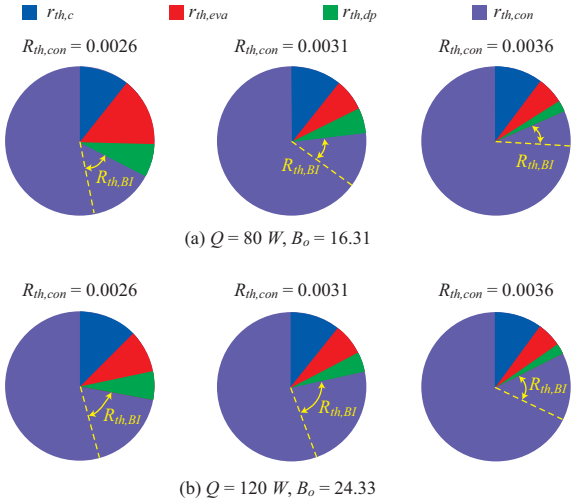

Fig. 9. Variations of composition of constituent thermal resistances for R_{th} by varying $R_{th,con}$ at fixed Q (B_o).

or $R_{th,con}$. The manner in which the compositions of the regional thermal resistances in R_{th} vary upon increasing Q (B_o) at fixed $R_{th,con}$ of (a) 0.0031 and (b) 0.0036 and upon increasing $R_{th,con}$ at fixed Q (B_o) of (a) 80 W (16.31) and (b) 120 W (24.33) are respectively shown in Figs. 8 and 9. In view of all the thermal resistance compositions affected by the flow conditions developed along the present TPLT, as shown in Figs. 8 and 9, $R_{th,con}$ constantly plays a dominant role in composing R_{th}. As reported previously [6, 25], the implicitly inclusive $R_{th,BI}$ in R_{th} remains noticeable. As B_o increases to increase the pressure and fluid temperature in the evaporator, the preheating effect is amplified by elevating $T_{f,eva}$ to increase $R_{th,BI}$. As a result, the percentage of $R_{th,BI}$ in R_{th} is increased by raising B_o at fixed $R_{th,con}$, as shown in Figs. 8(a) and (b). As B_o increases at fixed $R_{th,con}$, the

corresponding *Nu* increase leads to a corresponding reduction in the evaporator thermal resistance. By way of superheat increase over the boiling wall in the present evaporator channel, the dryness factor of vapor emitted from the evaporator accordingly increases, leading to a reduction in the pressure drop through the pipeline upstream of the condenser. Consequently, the fluid temperature drop corresponding to the reduced pressure drop through the pipeline between the evaporator and the condenser is reduced. Owing to the elevated boiling *Nu* and vapor dryness factor in the evaporator with increasing B_o, the percentages of $R_{th,eva}$ and $R_{th,dP}$ in R_{th} are both reduced even if the total thermal resistances simultaneously decrease as B_o increases, as shown in Fig. 8.

As $R_{th,con}$ increases at fixed B_o, the total thermal resistance is increased along with the enhanced significance of $R_{th,con}$ in composing R_{th}, as shown in Fig. 9. At each fixed Q (B_o), $R_{th,con}$ increases upon reducing the external cooling airflow rate to incur elevations of boiling *Nu*, superheat on boiling wall, and evaporator pressure (P^*). Even if R_{th} is increased by increasing $R_{th,con}$ at fixed B_o, the increased boiling *Nu* and dryness factor lead to reductions of the percentages of $R_{th,eva}$ and $R_{th,dP}$ in composing R_{th}, as shown in Fig. 9. The percentage of $R_{th,BI}$ in R_{th} systematically declines with increasing $R_{th,con}$, as shown in Figs. 9(a) and (b). Variations in $R_{th,con}$ cause varying trends of $R_{th,con}$, $R_{th,eva}$, $R_{th,dP}$, and $R_{th,BI}$, all of which contribute to R_{th}; these trends caused by varying $R_{th,con}$ are followed by all tested B_o values, the increase in B_o alleviates the degree of the impact of $R_{th,con}$ on the composition of R_{th}, as seen from a comparison of the results shown in Figs. 9(a) and (b).

With the presence of NCG in the present TPLT fitted with SRTTs in the evaporator, the boiling Nusselt numbers are reduced from the TPLT of the plain evaporator channel without NCG, as seen from the comparison in Fig. 7. This disparity elevates the percentage of $R_{th,eva}$ in composing R_{th} for the present TPLT, relative to the TPLT of the plain evaporator channel without NCG. However, the moderation of the boiling instabilities by the present twin SRTTs also leads to a reduced $R_{th,BI}/R_{th}$ ratio relative to those generated in the TPLT of plain evaporator channels without NCG (Chang et al., 2012). Thus, the comparable R_{th} performance levels between the present enhanced TPLT with NCG and the TPLT in the plain evaporator channel without NCG reflect the competing effects caused by fitting the twin SRTTs in the evaporator channel to reduce the $R_{th,BI}/R_{th}$ ratio and the increased $R_{th,eva}/R_{th}$ ratio from the references found in the TPLT of plain evaporator channels without NCG (Chang et al., 2012). This is demonstrated in Fig. 10, in which the variations of (a) $R_{th,BI}/R_{th}$ and (b) $R_{th,eva}/R_{th}$ against B_o for the pre-sent enhanced TPLT with NCG and the TPLT of the plain evaporator channel without NCG are compared. For these two TPLTs, the ratios of $R_{th,BI}/R_{th}$ are in the range of 0.075-0.385 and those of $R_{th,eva}/R_{th}$ are in the range of 0.025-0.11, as shown in Fig. 10. Clearly, the significance of $R_{th,BI}$ in composing R_{th} is greater than the $R_{th,eva}$ counterpart. Therefore, the moderation of the liquid surface oscillations by the present SRTTs, which consequently reduces the $R_{th,BI}/R_{th}$ ratios relative to those of the

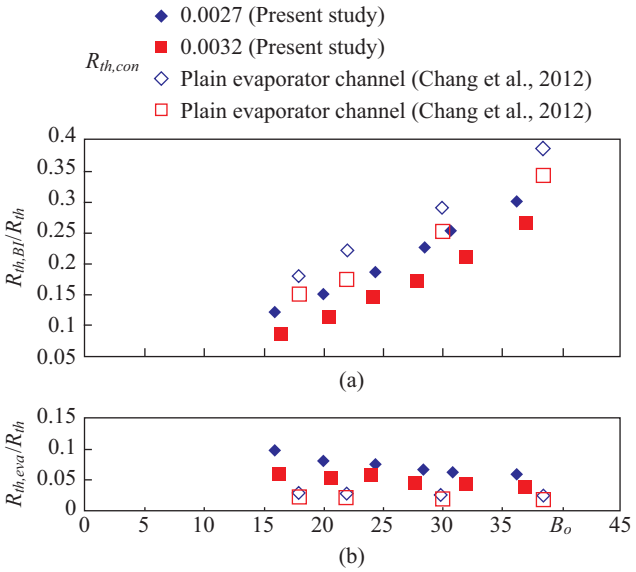

Fig. 10. Variations of (a) $R_{th,BI}/R_{th}$ and (b) $R_{th,eva}/R_{th}$ against B_o for TPLT with SRTTs and 40 vol% NCG and TPLT of plain evaporator without NCG (Chang et al., 2012).

plain channel counterparts as shown in Fig. 10(a), take precedence over the increased $R_{th,eva}/R_{th}$ ratios from the plain channel counterparts, as shown in Fig. 10(b). Nevertheless, in keeping with the results shown in Figs. 8 and 9, the increase in $R_{th,con}$ from 0.0027 to 0.0032 reduces the ratios of $R_{th,BI}/R_{th}$ and $R_{th,eva}/R_{th}$ at each fixed R_o for both TPLTs.

Fig. 11(a) shows a comparison of the total thermal resistances between the TPLT with NCG and SRTTs and the TPLT without NCG and SRTT (Chang et al., 2012) under different test conditions. As seen from the comparison in Fig 11(a) at fixed $R_{th,con}$ of 0.0027 or 0.0032, the total thermal resistances with six or four different B_o elements between the two TPLTs with and without SRTTs are noticeable. As $R_{th,con}$ for the present TPLT played a dominant role in composing R_{th}, the increase in $R_{th,con}$ at fixed *Bo* elevates the total thermal resistance, even though both composing percentages of $R_{th,eva}$ and $R_{th,dP}$ in R_{th} are reduced by increasing $R_{th,con}$. As B_o increases at fixed $R_{th,con}$, the total thermal resistances shown in Fig. 11(a) are reduced owing to the corresponding $R_{th,eva}$ and $R_{th,dP}$ reductions. Fig. 11(a) also shows a comparison of the R_{th} data measured from the TPLT of the plain evaporator without NCG (Chang et al., 2012). With $R_{th,con}$ = 0.0027 or 0.0032, the total thermal resistances for the present TPLT at all tested B_o values are slightly lower than the plain channel counterparts (Chang et al., 2012), as shown in Fig. 11(a). Based on the comparative results shown in Fig. 2, the presence of twin SRTTs considerably suppresses the oscillating amplitudes of the liquid level relative to those in the plain channel counterparts. Meanwhile, the contributions of $R_{th,BI}$ for composing R_{th} are more significant than the roles of $R_{th,eva}$, as shown in Figs. 8 and 9. Following the consistent trend of the B_o-driven R_{th} decays at tested $R_{th,con}$, the R_{th} data for the present TPLT with SRTTs and 40 vol% NCG are

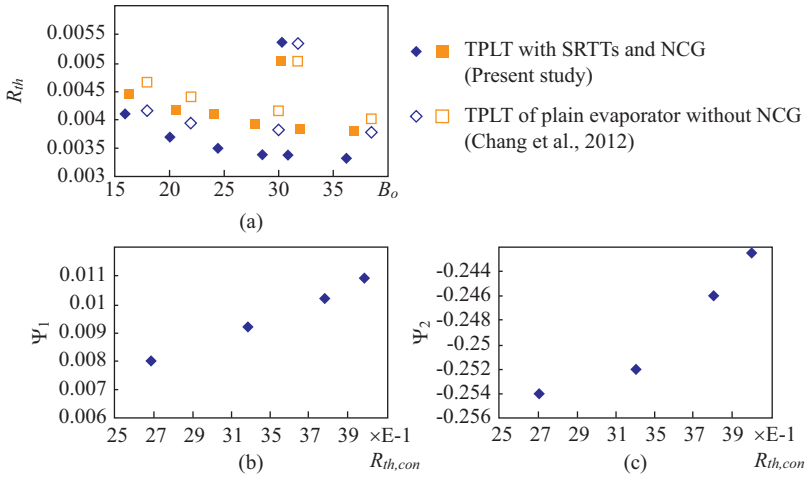

Fig. 11. Variations of (a) R_{th} against Bo at fixed $R_{th,con}$ and (b) Ψ_1 and (c) Ψ_2 variations against $R_{th,con}$.

correlated by the general power-law function in Eq. (20):

$$R_{th} = \Psi_1 \times B_o^{\Psi_2} \tag{20}$$

As shown in Fig. 11(a), the Ψ_1 coefficient and Ψ_2 exponent in Eq. (20) are functions of $R_{th,con}$. For finding the R_{th} correlation, the variations of Ψ_1 and Ψ_2 against $R_{th,con}$ are examined, as shown in Figs. 11(b) and (c). Clearly, Ψ_1 and Ψ_2 values can be well correlated as linear and quadratic functions of $R_{th,con}$, as shown in Eqs. (21) and (22), respectively.

$$\Phi_1 = 9.6\text{E-}4 + 2.59 \times R_{th,con} \tag{21}$$

$$\Phi_2 = -0.179 - 55.12 \times R_{th,con} + 10108 \times R_{th,con}^{\ 2} \tag{22}$$

With a specified $R_{th,con}$ in Eqs. (21) and (22) for defining Ψ_1 and Ψ_2, the correlative R_{th} is obtained after substituting B_o into Eq. (20). A comparison of all R_{th} data against the correlation results evaluated using Eqs. (20)-(22) shows maximum discrepancies of ±20%. In view of the comparative R_{th} results between the present TPLT with SRTTs and 40 vol% NCG and the TPLT of plain evaporators without NCG, shown in Fig. 11(a), the decreased R_{th} achieved by reducing $R_{th,BI}$ using twin SRTTs can be adopted to counteract the unfavorable effects of NCG on the thermal performance improvement of the thermosyphon loop.

IV. CONCLUSIONS

The present experimental study used twin SRTTs along the evaporator channel of a sub-atmospheric two-phase thermosyphon loop with 40 vol% NCG. The impacts of B_o and $R_{th,con}$ on the boiling flow structure, boiling heat transfer rate, thermal resistance composition, and total thermal resistance were examined, and the following conclusions were derived from this study.

(1) The increase in B_o or $R_{th,con}$ directed the transition of the boiling flow structures in the rectangular evaporator channel with twin SRTTs from intermittent slug flow → intermittent churn flow → continuous churn flow → continuous bubbly flow. The interfacial boundaries segregating the flow regimes in the boiling flow map were negligibly affected by the SRTT inserts. The oscillations of the liquid surface in the evaporator channel with the present twin SRTTs were considerably alleviated relative to those in the plain evaporator channel to moderate the preheating effects caused by such boiling instabilities.

(2) The regionally averaged Nusselt numbers followed the order of liquid pool > intermittent > vapor regimes, and they increased upon increasing B_o or $R_{th,con}$ owing to the responsive interfacial transition of the boiling flow structures in the present evaporator. The increase in boiling Nu caused by increasing $R_{th,con}$ is mainly attributed to the elevated evaporator pressure and superheated temperature at fixed B_o.

(3) With the presence of 40 vol% NCG in the present TPLT, the boiling heat transfer rates were reduced relative to those in the plain evaporator channel without NCG.

(4) At each fixed B_o, the present R_{th} increased with the increase in $R_{th,con}$ but decreased upon increasing B_o at fixed $R_{th,con}$. As the moderations of $R_{th,BI}/R_{th}$ outweighed the elevations of $R_{th,eva}/R_{th}$ for the present TPLT with SRTTs and NCG, R_{th} for the present TPLT was reduced relative to that of the TPLT with the plain evaporator without NCG. The reduced $R_{th,BI}$ by fitting SRTTs in the evaporator channel was the main factor that counteracted the unfavorable NCG effects for thermal performance improvement.

(5) Two sets of empirical correlations using B_o and $R_{th,con}$ as the controlling parameters for calculating the regionally averaged Nu over the liquid pool, intermittent, and vapor regions in the present boiling channel and the total thermal resistance were devised to represent all the data generated in the present study.

V. NOMENCLATURE

English symbols

A heater foil area (m^2)
B_o boiling number = $QC_{pL}/(h_{fg}k_L d)$
Cp constant-pressure specific heat of liquid coolant ($Jkg^{-1}K^{-1}$)
d evaporator channel hydraulic diameter of TPLP (m)
h boiling convective heat transfer coefficient = $Q/[A \times (T_w - T_f)]$
h_{fg} latent heat of test coolant (Jkg^{-1})
k_L thermal conductivity of coolant (liquid) ($Wm^{-1}K^{-1}$)
$\dot{m}_a$ mass flow rate of external cooling airflow through condenser (kgs^{-1})
P pressure (Nm^{-2})
P_{cr} critical pressure of working fluid (water) (Nm^{-2})
P_E saturated pressure of evaporator (Nm^{-2})
Pi pitch of twisted tape over 180° turn (m)
P^* dimensionless evaporator pressure = P_E/P_{cr}
Q heater power (W)
q convective heat flux (Wm^{-2}) = Q/A
r_{th} total thermal resistance of TPLT = $(T_E - T_{a,i})/Q(kW^{-1})$
$r_{th,BI}$ boiling instability thermal resistance = $\Delta T_{,BI}/Q(kW^{-1})$
$r_{th,c}$ contact thermal resistance (kW^{-1}) = $\Delta T_{,c}/Q$
$r_{th,con}$ condenser thermal resistance (kW^{-1})
$r_{th,dP}$ pressure drop thermal resistance = $\Delta T_{,dP}/Q$ (kW^{-1})
$r_{th,eva}$ evaporator thermal resistance = $\Delta T_{,eva}/Q$ (kW^{-1})
$R_{th,BI,c,con,dp,eva}$ dimensionless thermal resistance = $k_L d \cdot r_{th,BI,c,con,dp,eva}$
$T_{a,i}$ airflow entry temperature of condenser (K)
$T_{a,o}$ airflow exit temperature of condenser (K)
T_E temperature of electrical heater foil (K)
T_f local evaporator fluid temperature (K)
T_{sat} saturation temperature (K)
T_w wall temperature (K)
$\Delta T_{,c}$ temperature drop from heater foil to evaporator wall (K)
$\Delta T_{,ev}$ temperature drop from evaporator wall to fluid in evaporator (K)
$\Delta T_{,dP}$ temperature drop from fluid in evaporator to condenser entrance (K)
$\Delta T_{,BI}$ temperature rise from condenser exit to evaporator entrance (K)
W_T width of twisted tape (m)
y twist pitch ratio of twisted tape = (Pi/W_T)

Greek Symbols

φ, Ψ, Φ correlative functions

ACKNOWLEDGEMENT

This work was financially supported by grant no. MOST105-2221-E-022-002 from the Ministry of Science and Technology, Taiwan, and AVC Company.

REFERENCES

Bowers, M. B. and I. Mudawar (1994). Two-phase electronic cooling using mini-channel and macro-channel heat-sinks - part II, flow rate and pressure drop constraints. ASME J. Electronic Packaging 116, 298-305.

Chang, S. W., D. C. Lo, K. F. Chiang and C. Y. Lin (2012). Sub-atmospheric boiling heat transfer and thermal performance of two-phase loop thermosyphon. Int. J. Experimental Thermal and Fluids Science 39, 134-147.

Chang, S. W. and C.Y. Lin (2013). Thermal performance improvement with scale imprints over boiling surface of two-phase loop thermosyphon at sub-atmospheric conditions. International Journal of Heat and Mass Transfer 56, 294-308.

Cooper, M. G. (1984). Saturation nucleate pool boiling, a simple correlation. International Chemical Engineering, Symposium Series 86, 785-792.

Editorial Board of ASME Journal of Heat Transfer (1993). Journal of heat transfer policy on reporting uncertainties in experimental measurements and results. ASME J. Heat Transfer 115, 5-6.

Figus, C., Y. Le Bray, S. Bories and M. Prat (1999). Heat and mass transfer with phase change in a porous structure partially heated: continuum model and pore network simulations. International Journal of Heat and Mass Transfer 42, 1446-1458.

He, J., G. Lin, L. Bai, J. Miao, H. Zhang and L. Wang (2013). Effect of non-condensable gas on startup of a loop thermosyphon. International Journal of Thermal Sciences 72, 184-194.

He, J., G. Lin, L. Bai, J. Miao, H. Zhang and L. Wang (2014). Effect of non-condensable gas on steady-state operation of a loop thermosyphon. International Journal of Thermal Sciences 81, 59-67.

Huang, J., L. Wang, J. Shen and C. Liu (2016). Effect of non-condensable gas on the start-up of a gravity loop thermosyphon with gas–liquid separator. Experimental Thermal and Fluid Science 72, 161-170.

Kandlikar, S. G. (2002). Fundamental issues related to flow boiling in mini-channels and micro-channels. Experimental Thermal Fluid Sciences 26, 389-407.

Khodabandeh, R. and B. Palm (2002). Influence of system pressure on the boiling heat transfer coefficient in a closed two-phase thermosyphon loop. International Journal of Thermal Sciences 41, 619-624.

Khodabandeh, R. (2005). Pressure drop in riser and evaporator in an advanced two-phase thermosyphon loop. International Journal of Refrigeration 28, 725-734.

Khodabandeh, R. and R. Furberg (2010) Instability, heat transfer and flow regime in a two-phase flow thermosyphon loop at different diameter evaporator channel. Applied Thermal Engineering 30, 1107-1114.

Niro, A. and G. P. Baretta (1990). Boiling regimes in a closed two-phase thermosyphon. International Journal of Heat and Mass Transfer 33, 2099-2110.

Nishikawara, M. and H. Nagano (2017). Optimization of wick shape in a loop heat pipe for high heat transfer. International Journal of Heat and Mass Transfer 104, 1083-1089.

Prado-Montes, P., D. Mishkinis, A. Kulakov, A. Torres and I. Pérez-Grande (2014). Effects of non condensable gas in an ammonia loop heat pipe operating up to 125°C. Applied Thermal Engineering 66, 474-484.

Randeep, S., A. Aliakbar and M. Masataka (2010). Operational characteristics of the miniature loop heat pipe with non-condensable gases. International Journal of Heat and Mass Transfer 53, 3471-3482.

Siedel, B., V. Sartre and F. Lefevre (2015). Literature review: Steady-state modelling of loop heat pipes. Applied Thermal Engineering 75, 709-723.

Tadrist, L. (2007). Review on two-phase flow instabilities in narrow spaces. International Journal of Heat and Fluid Flow 28, 54-62.

Vasiliev, L. L. (2005). Heat pipes in modern heat exchangers. Applied Thermal Engineering 25, 1-19.

Vasiliev, L. L., L. P. Grakovich, M. I. Rabetsky, L. L. Jr. Vassiliev and A. S. Zhuravlyov (2017). Thermosyphons with innovative technologies. Applied Thermal Engineering 111, 1647-1654.